A Magnetically-Actuated Coiling Soft Robot With Variable Stiffness

Peter Lloyd, Theodosia Lourdes Thomas, *Graduate Student Member, IEEE*, Venkatasubramanian Kalpathy Venkiteswaran, *Member, IEEE*, Giovanni Pittiglio, James H. Chandler, *Member, IEEE*, Pietro Valdastri, *Fellow, IEEE*, and Sarthak Misra, *Senior Member, IEEE*

***Abstract*—Soft and flexible magnetic robots have gained significant attention in the past decade. These robots are fabricated using magnetically-active elastomers, are capable of large deformations, and are actuated remotely thus allowing for small robot size. This combination of properties is appealing to the minimally invasive surgical community, potentially allowing navigation to regions of the anatomy previously deemed inaccessible. Due to the low forces involved, one particular challenge is functionalizing such magnetic devices. To address this limitation we introduce a proof-of-concept variable stiffness robot controlled by remote magnetic actuation, capable of grasping objects of varying sizes. We demonstrate a controlled and reversible high deformation coiling action induced via a transient homogeneous magnetic field and a synchronized sliding nitinol backbone. Our soft magnetic coiling grasper is visually tracked and controlled during three experimental demonstrations. We exhibit a maximum coiling deformation angle of 400°.**

***Index Terms*—Grasping, magnetic continuum robots, soft robots, surgical robotics, magnetic actuation, continuum manipulators.**

I. Introduction

Soft magnetic robots, due to an inherent reduction in traumatic anatomical forces, display the potential to supersede traditional mechanically-actuated minimally invasive surgical instruments [1], [2], [3]. The ability of these robots to manoeuvre through delicate and critical anatomy in a minimally invasive manner is key to improving the feasibility and success of many treatments [4]. Magnetic actuation allows devices to be composed of softer materials as forces and torques can be applied directly to embedded magnetic material as opposed to lengthwise force transmission [5], [6]. Furthermore, this class of rapid and clinically safe actuation eliminates the need for on-board power transmission systems (such as electrical or pneumatic) allowing easy miniaturization [7].

In order to introduce shape-programmability, magnetically-hard particles with high coercivity can be incorporated into mechanically soft materials capable of large deformations [8], [9], [10]. This system is capable of creating complex time

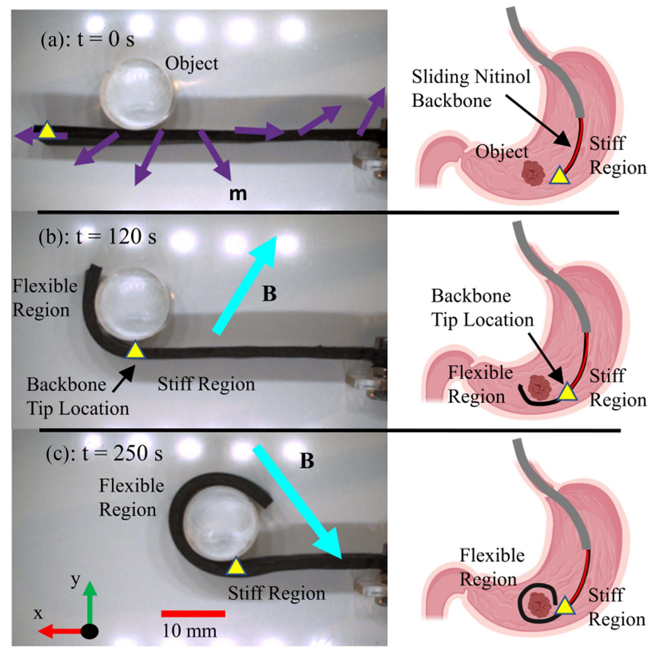

Fig. 1. Three representative instances taken from the supporting video (left, t = 0, 120, 250 s) shown alongside a clinically relevant application - grasping for removal of an excised stomach tumour (right). (a) The sliding nitinol backbone is fully inserted (tip of backbone shown as yellow triangle on the left and red overlay on the right) - the stiff region will not respond to actuation. Magnetization (**m**) is shown here by purple arrows. (b) The wire-frame is partially retracted allowing deformation of the "Flexible Region". This is actuated via a homogeneous magnetic field (**B**) shown as the turquoise arrows. The "Stiff Region" retains its backbone support. (c) The wire-frame is further retracted as the applied field is rotated. This grasping pose would be unachievable without the sliding nitinol backbone.

Manuscript received 31 October 2022; accepted 27 March 2023. Date of publication 5 April 2023; date of current version 21 April 2023. This letter was recommended for publication by Associate Editor E. D. Diller and Editor J. Burgner-Kahrs upon evaluation of the reviewers comments. This work was supported in part by the Engineering and Physical Sciences Research Council (EPSRC) under Grants EP/R045291/1 and EP/V009818/1, and in part by the European Research Council (ERC) through European Union's Horizon 2020 Research and Innovation Programme under Grant 818045, and in part by the Netherlands Organization for Scientific Research (NWO) through Innovational Research Incentives Scheme VIDI: SAMURAI under Grant 14855. *(Peter Lloyd and Theodosia Lourdes Thomas contributed equally to this work.) (Corresponding author: Peter Lloyd.)*

Peter Lloyd, Giovanni Pittiglio, James H. Chandler, and Pietro Valdastri are with the Storm Lab, School of Electronic and Electrical Engineering, University of Leeds, LS2 9JT Leeds, U.K. (e-mail: men9prl@leeds.ac.uk; giovanni.pittiglio@childrens.harvard.edu; j.h.chandler@leeds.ac.uk; p.valdastri@leeds.ac.uk).

Theodosia Lourdes Thomas and Venkatasubramanian Kalpathy Venkiteswaran are with the Surgical Robotics Laboratory, Department of Biomechanical Engineering, University of Twente, 7500 AE Enschede, The Netherlands (e-mail: t.l.thomas@utwente.nl; v.kalpathyvenkiteswaran@utwente.nl).

Sarthak Misra is with the Surgical Robotics Laboratory, Department of Biomechanical Engineering, University of Twente, 7500 AE Enschede, The Netherlands, and also with the Surgical Robotics Laboratory, Department of Biomedical Engineering, University of Groningen and University Medical Centre Groningen, 9713 GZ Groningen, The Netherlands (e-mail: s.misra@utwente.nl).

This letter has supplementary downloadable material available at https://doi.org/10.1109/LRA.2023.3264770, provided by the authors.

Digital Object Identifier 10.1109/LRA.2023.3264770

varying shapes at small scales as magnetic field control inputs can be specified in magnitude, direction and spatial gradient [11]. Magnetic soft continuum structures can also be fabricated with a continuous lengthwise magnetization profile thus generating spatially resolved deformations [11]. A range of applications have been demonstrated using this approach [7] including, amongst other applications, autonomous navigating catheters [6], cilia-like shape forming structures [11], untethered swimmers [10], shape forming catheters [12], [13], and untethered grippers [14].

Softness represents a clear advantage for medical tools [15], however, this can also be problematic when it comes to performing functional tasks. As such, variable stiffness becomes a highly desirable feature such as the magnetic catheter with conductive shape memory polymer demonstrated in [16]. There are many approaches to achieve stiffening, most commonly; geometric changes such as modifying the cross-sectional profile, elastic changes such as phase transition or jamming and antagonistic actuation [17]. The typical motive for stiffening in continuum robots, however, is to shape-lock after actuation [18]. Our design, on the contrary, offers a system which is shape locked prior to actuation and mechanical stiffening during the coiling phase is provided by the magnetic actuation itself. This is a novel stiffener/actuator arrangement with potential for future development using alternative stiffening technologies such as the temperature based bulk material property varying systems in [19] and [20] or the magneto-rheological stiffening demonstrated in [21]. Low melting point induced variable stiffness was exploited in [19] to achieve stable high deformation bending ($\approx 270°$) under magnetic actuation. Here we demonstrate fully wrapped deformation ($>360°$) for a high grip strength grasping mode in a manner with greater potential for miniaturization.

In this proof-of-concept work, we employ material variable stiffness in the form of a sliding nitinol backbone which offers a stiffness change factor of close to 800. This movement is synchronistically controlled within a closed-loop with a time-varying actuating field (Fig. 1) for the novel purpose of constraining some proximal length of our robot against deformation whilst we actuate the remaining distal length (Fig. 2). This allows us to apply otherwise unstable combinations of magnetization and actuating field to achieve a forward time marching deformation, fully dependent on the previous pose. Consequently, we generate a higher strain equilibrium and achieve circular deformations greater than one full revolution. Our conceptual design shares some similarities with the pre-curved elastomers of e.g. [22]. However, the actuating magnetic field allows us to exploit soft elastomeric construction without a corresponding reduction in grasp strength.

As a proof-of-concept we have applied our innovation to the demonstrative example of reversible coiling for grasping or delivery. There exists a clinical role for minimally invasive cargo retrieval or delivery systems, either untethered [23], [24] or via endoscopic manipulators [25]. Furthermore, there is a demonstrable appetite for the automation and miniaturization of both approaches [26], [27]. Other grasping type designs have been demonstrated in the literature such as the pneumatically actuated systems in [28] and the electromagnetic coil of [29]

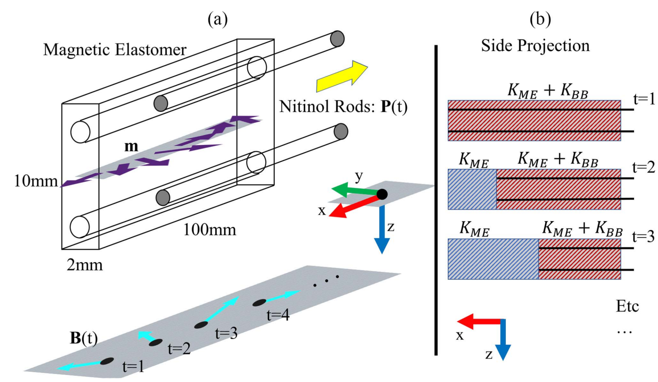

Fig. 2. Schematic of the underlying design and actuation strategy for arbitrary time steps (t = 1, 2, 3..). (a) The elastomer is magnetized (**m**), shown as purple arrows, in the x-y plane (shown in grey) in a spatially sinusoidal fashion along the length of the x-axis. A temporally sinusoidal actuating field (**B**(t), turquoise arrows) is applied (also in the x-y plane), as the nitinol rod backbone is withdrawn (**P**(t), yellow arrow). (b) This controlled augmentation of the unconstrained, and therefore lower stiffness, length of the VSR allows higher strain energy states to be achieved. K_{ME} and K_{BB} are the elastic stiffness of the magnetic elastomer and the nitinol backbone, respectively.

but these systems are all limited to varying extents in their minimum size. Our high deformation, variable stiffness approach offers the potential for increased grasp strength per unit size over magnetic forceps-like designs [30] whilst still displaying potential for miniaturization. We demonstrate our grasping motion for cylinders of diameters ranging from 10-15 mm. Whilst this investigation is still very much at the feasibility stage of development and these cylindrical objects are therefore largely arbitrary, there is indication that these shapes and sizes would have medical relevance [31].

The contribution of this letter is the actuation of a potentially unstable magnetic robot with variable stiffness. Synchronized actuation and variable stiffness combine to achieve stable, large deformation shape forming. To prove the necessity of the inclusion of the sliding nitinol backbone, we also demonstrate the unsuccessful actuation of the robot without the inclusion of stiffening wires. Following experimental evaluations with different geometries, this system is implemented in an 80 mm long, 10 mm x 2 mm cross-section tongue-like robot which grasps and releases arbitrary objects via coiling.

II. The Variable Stiffness Robot

In this section, we detail the analytical design principles, the fabrication technique and the dual material characterization of our tongue-like, variable stiffness robot (VSR).

A. Analytical Design - Elastic Torque

We represent the flexible, unsupported region of the VSR as a serial chain of rigid links connected by planar (1 Degree of Freedom) rotational joints as a simplification of [32] and [33]. Any desired shape can be represented as a vector of joint angles $\mathbf{q}$ where the length of $\mathbf{q}$ is determined by the granularity of discretization (individual link length l) and the unconstrained length of the VSR, itself a function of time ($L = L(t)$). Elastic joint torque is given as

$$\boldsymbol{\tau}_{elas} = \frac{K\mathbf{q}}{l}, \tag{1}$$

where l is the virtual link length and K is the elastic stiffness given by

$$K = E_{ME}I_{ME} + E_{BB}I_{BB}, \tag{2}$$

with E_{ME} and I_{ME} as the Young's modulus and the second moment of area for bending of the rectangular cross-section magnetic elastomer, and E_{BB} and I_{BB} are those of the circular cross-section backbone, respectively (See Fig. 2)

$$I_{ME} = \frac{wh^3}{12}, \tag{3}$$

$$I_{BB} = \frac{n\pi}{4}r^4, \tag{4}$$

with w as the elastomer width, h as the elastomer height, r as the radius of the support rods, and n as the number of support rods. When the nitinol backbone is withdrawn $E_{BB} = 0$ and the mechanical stiffness drops dramatically.

B. Analytical Design - Magnetic Torque

A magnetic dipole with moment $\mathbf{m}$ in a homogeneous field $\mathbf{B}$(t) will experience a resultant magnetic torque proportional to applied field strength

$$\boldsymbol{\tau}_{mag}(t) = \mathbf{m} \times \mathbf{B}(t), \tag{5}$$

where $\mathbf{B}(t)$, $\mathbf{m}$, $\boldsymbol{\tau}_{mag}(t) \in \mathbb{R}^3$ (If $\mathbf{B}$ and $\mathbf{m}$ are constrained to the x-y plane then the cross product becomes *effectively* scalar). The body torque acting on any discretized segment (virtual link) of the VSR as a consequence of the interaction of the actuating magnetic field, and the *deformed* magnetization of that region of doped elastomer will produce deformation, and therefore be counteracted by the elastic properties of the material.

C. Analytical Design - Torque Balance

Assuming gravity to be zero, we can balance the elastic torque at any given virtual joint (i, in a VSR of N virtual joints) with the aggregation of magnetic torques on every distal virtual link in the VSR at any given time step

$$\tau_{i,elas} = \sum_{n=i}^{N} \boldsymbol{\tau}_{n,mag}. \tag{6}$$

As illustrated in Fig. 3, we can define our desired shape as some proportion of a circle. The joint array q for a full circle of deformation becomes N equal joints of $\frac{360}{N}^{\circ}$, where q increases in length by one entry with each time step from $t = 0$ to $t = N$. Anything proximal to the joint of interest will be constrained by the backbone and is assumed to be rigid (See Section II-E).

Inverting the aggregation of (6) over all time steps would give non-unique solutions for $\mathbf{m}$ and $\mathbf{B}$ - the necessary combination of fields and magnetizations can be rotated about z whilst still producing feasible outputs. By implementing the constraint that the distal magnetization must be axial (to give a reliable reference direction for the magnetic field vector), a unique solution exists for any set of joint angle arrays. A further constraint imposed by the magnetization process was that all segment magnetizations must be within 60° of all their neighbouring segment magnetizations. This solution was determined using the Genetic Algorithm (GA, Global Optimization Toolbox, Matlab version R2021b) to generate discretized magnetization profiles and time-stepping actuating fields.

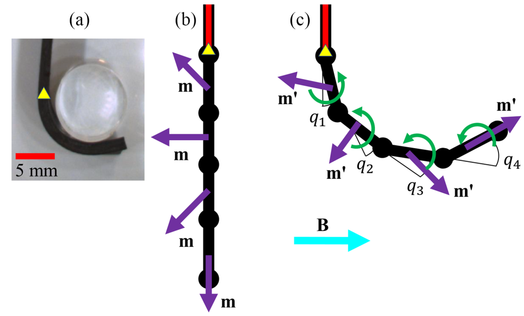

Fig. 3. (a) A representative pose of the VSR with the tip location of the sliding nitinol backbone indicated by the yellow triangle and the backbone supported region shown as red overlay. (b) Illustratively discretized into four rigid links with referential magnetizations ($\mathbf{m}$) shown as purple arrows. (c) Deformed magnetization ($\mathbf{m}'$) shown again as purple arrows, resultant magnetic torques as green arrows, applied field ($\mathbf{B}$) as turquoise arrow and deformed joint angles as q_i, $i \in [1, 4]$.

It was noted that the output of the optimization - magnetization profiles and applied fields - due to the special case of a fully circular desired deformation, were sinusoidal in nature. The magnetization sinusoid running spatially along the long axis of the robot, as can be observed in Figs. 2 and 3, and the actuating field sinusoid rotating as a function of time. This result allowed us to fit an analytical form to both the magnetization profile, described next, and to the initial actuating field, described in Section III-C.

The driving variable here is the *bending radius* (r) and is defined as the radius of the circle which is formed by the array of equal desired joint angles, so, taking q_{des} as a scalar from the joint angle array and with l as the virtual link length gives

$$r = \frac{l}{2\sin\left(q_{des}\right)}. \tag{7}$$

Consequentially, defining position along the robot length from the tip as S, the magnetization ($\mathbf{m}$) at any point along the robot is defined as

$$\mathbf{m} = |\mathbf{m}|\mathrm{rot}_z\left(\frac{S}{\pi r}180^{\circ}\right)\hat{\mathbf{x}}, \tag{8}$$

with $\hat{\mathbf{x}}$ the unit vector in the x direction, and $\mathrm{rot}_z(\cdot) \in SO(3)$ the rotation matrix about the z-axis. The resultant rotational speed of the actuating field is a function of the speed of retraction of the backbone.

Due to desired deformations greater than 360°, the presented solutions have sacrificed design flexibility and are capable of generating only the target circular shapes reported (with the exception of the lower energy deformation shown in Fig. 5). Other profiles could be generated using the same process but

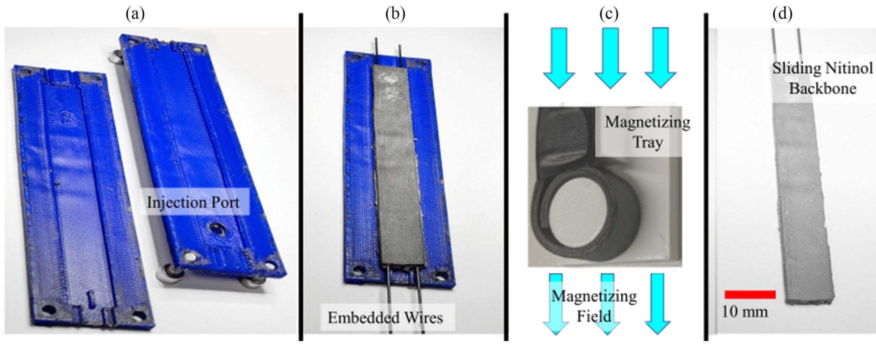

Fig. 4. The key steps in the process of fabrication. (a) A mold is 3D printed in Polylactic acid. The injection port can be seen here. (b) 0.75 mm diameter nitinol wires are embedded lengthways and doped silicone is injected and cured. (c) The specimen is demolded, wrapped around a magnetizing tray (shown in grey) of specific bending radius and exposed to a saturating magnetizing field, shown here as turquoise arrows. (d) 0.5 mm diameter nitinol wires are inserted to act as the sliding backbone.

would require diverse magnetization solutions as demonstrated in [10], [12].

D. Fabrication

The manual fabrication process is outlined in Fig. 4 and is based on [12]. A split mold was 3D printed (RS-F2-GPGR-04, Formlabs, USA) into which 0.75 mm diameter nitinol wires are embedded, and the arrangement is bolted and glued shut. The elastomer (Ecoflex-0030, Smooth-On Inc, USA) was mixed with neodymium-iron-boron (NdFeB) microparticles with an average diameter of 5 µm (MQFP-B+, Magnequench GmbH, Germany) in a 1:1 mass ratio giving a saturated remnance of 120 mT [34]. This composite was mixed and degassed in a high vacuum mixer (ARV-310, THINKYMIXER, Japan) at 1400 rpm, 20.0 kPa for 90 seconds. The mixture was injected into the mold and cured at room temperature for four hours. Upon demolding, the 0.75 mm diameter nitinol rods are removed.

The specimens were then secured in a circular 3D printed magnetizing mold before being subjected to a saturating uniform field of 4.644 T (ASC IM-10-30, ASC Scientific, USA). The bending radius of the circle about which the specimen is wrapped during magnetization is described in Section II-C and discussed in Section V. For Sample 1 this parameter was 7.5 mm and for Sample 2 it was 5 mm.

Finally, the holes from which the 0.75 mm diameter rods were removed are filled with free sliding 0.5 mm diameter nitinol backbone rods. The robot body is capable of large elastic strains before the onset of plastic deformation. Consequently, the post magnetization unactuated state remains uncurved, with or without the nitinol backbone.

E. Variable Stiffness Characterization

Using Ecoflex-0030 (Smooth-On Inc, USA) doped at 100% by weight gives $E_{ME} = 100$ kPa [34]. $E_{BB} = 50$ GPa [35] and from (3) and (4) with $w = 2$ mm, $h = 10$ mm, $r = 0.25$ mm and n = 2 gives the elastic stiffness of the nitinol backbone (K_{BB}) and the magnetic elastomer (K_{ME}) as

$$K_{BB} = 3 \times 10^{-4}\ \mathrm{Nm}^2,$$
$$K_{ME} = 7 \times 10^{-7}\ \mathrm{Nm}^2.$$

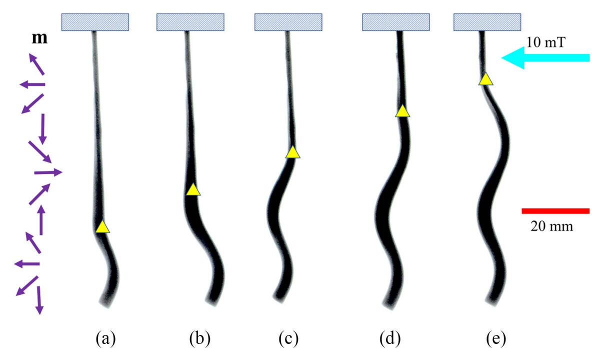

Fig. 5. The variable stiffness robot (VSR), magnetized according to the purple arrows ($\mathbf{m}$) and constrained at the base (blue rectangles), is shown under static one-dimensional magnetic actuation (turquoise arrow) for various insertions of sliding nitinol backbone signified here by yellow triangles. (a) Distal 20 mm unconstrained. (b) Distal 30 mm unconstrained. (c) Distal 40 mm unconstrained. (d) Distal 50 mm unconstrained. (e) Distal 60 mm unconstrained. Due to the stiffness change factor, deformation can only occur in the unconstrained region of the VSR. This shows the lowest energy state of the sinusoidally magnetized VSR. When unactuated, the device (constrained or unconstrained) exhibits a straight profile being subject to only gravitational forces.

This gives an analytical stiffness change factor of 765. In practice, no measurable bending deformation is observed at fields up to 50 mT in the backbone supported region of the VSR. Fig. 5 shows the VSR in a static actuating field with incrementally adjusted support positions - the point at which the backbone reaches is marked with a yellow triangle. This clearly demonstrates the absence of bending in any of the proximal, supported regions. Furthermore, Fig. 5 shows the lowest energy state of the sinusoidally magnetized VSR. Without forcing the robot into the coiled higher energy state using correctly coupled backbone retraction *and* time-varying applied fields we cannot achieve the large deformations with which we functionalize the system. The supporting video: S1 also illustrates the failure of the VSR to coil around an object and uncoil when the actuating field is applied sinusoidally but the sliding nitinol backbone is absent.

III. Controlled Actuation

In this section, we demonstrate a proof-of-concept functionalization of our VSR.

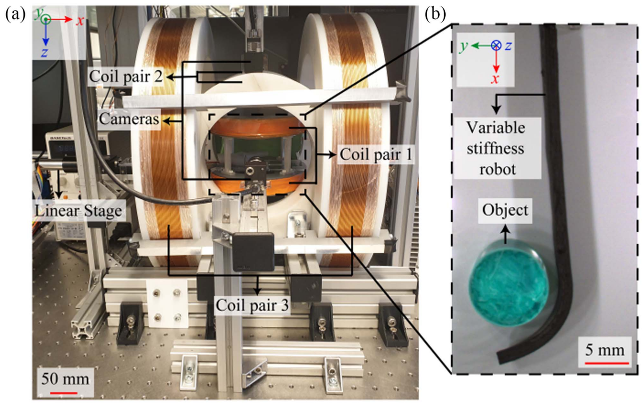

Fig. 6. The actuation system showing (a) PaCMag - 3D electromagnetic coil setup and the linear stage. (b) Top view of the variable stiffness robot grasping an object in the workspace.

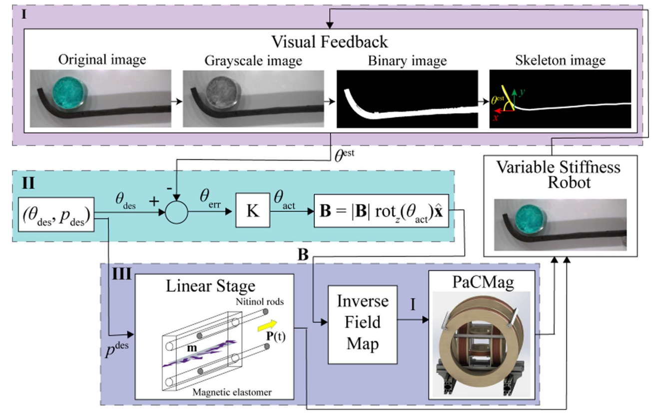

Fig. 7. Closed-loop control of the variable stiffness robot (VSR) summarized in three blocks: (I) The tip angle (θ_{est}) of the VSR is estimated from the camera and sent as feedback to the controller. (II) A proportional control calculates the magnetic field (**B**) and its angle (θ_{act}) to be applied from the error (θ_{err}) between the desired (θ_{des}) and estimated (θ_{est}) tip angles. (III) PaCMag applies the magnetic field by computing the required current (I) from the inverse field map. The linear stage moves the nitinol backbone to a position (p_{des}) updated based on the current desired tip angle (θ_{des}).

A. Actuation Systems

A 3-D electromagnetic coil setup (PaCMag) is used with a cylindrical workspace of equal radius and height of 65 mm as shown in Fig. 6, [36]. It has three coil pairs which can generate linearly independent uniform magnetic fields up to 55 mT. Experiments are conducted by supporting the VSR horizontally in the workspace of PaCMag and a linear stage (LX20, Misumi Group Inc., Tokyo, Japan) fixed at the base controls the movement of the nitinol backbone. A camera situated at the top captures the motion of the VSR.

B. Visual Sensory Feedback

An image processing algorithm is developed in OpenCV to track the tip angles of the VSR in 2D using camera images. Firstly, the original image is converted to a grayscale image. The shape of the VSR is extracted from the background by converting the grayscale image to a binary image. A threshold operation in the range of 60-255 is performed to convert the grayscale pixels and obtain a binary image of the VSR. Secondly, a skeletonization algorithm based on Zhang-Suen thinning algorithm is performed on the binary image to extract the skeleton of the VSR [37]. The tip of the VSR is then identified as the end point of the skeleton. Lastly, the slope of the end segment is calculated to find the tip angle of the VSR, this is used as feedback for the closed-loop controller.

C. Calculation of Actuating Field

We implemented a linear controller with a gain parameter fixed throughout at 10% based on experimental observations. The one dimensional error function is derived as the difference between the estimated tip angle ($\theta_{\text{est}} \in \mathbb{R}^1$) from Section III-B and the desired tip angle ($\theta_{\text{des}} \in \mathbb{R}^1$). This desired tip angle is predefined as a vector assembled from a circle discretized into small increments, for example, $\theta_{\text{des}} = [10, 24, 38, \ldots, 206, 220]^\circ$. The actuating field ($\mathbf{B} \in \mathbb{R}^3$) is set to a constant magnitude ($|\mathbf{B}| = 20$ mT) and the control variable is the angle of the applied field (θ_{act}) relative to the x-axis (see Fig. 7).

$$\mathbf{B} = |\mathbf{B}|\text{rot}_z(\theta_{\text{act}})\hat{\mathbf{x}}. \tag{9}$$

The applied field angle at time (t) is updated according to the error function ($\theta_{err} = \theta_{\text{des}} - \theta_{\text{est}}$) until the tolerance ($\theta_{err} < 5^\circ$) is attained as shown below,

$$\theta_{\text{act}}(t) = \text{K}_\text{I}\theta_{\text{err}}(t) + \theta_{\text{act}}(t-1), \tag{10}$$

where K_I is the integral gain. The system then retracts the nitinol backbone one increment before advancing to the next desired tip angle. Due to the elastomeric nature of the material, soft contact with the obstacle and the relatively slow (quasi-static) speed of rotation of the magnetic field, a feed-back only, integral controller is sufficient for this demonstration.

D. Calculation of Retracting Stage Position

By synchronizing the withdrawal of the backbone support with the rotation of the actuating field we avoid any twisting or warping instabilities. The time-varying position of the nitinol backbone ($P(t)$) is defined as: $P(t) = L - p_{\text{des}}(t)$, where L is the total robot length and the incremental position ($p_{\text{des}}(t)$) is linearly correlated to the desired angle of deformation ($\theta_{\text{des}}(t)$) via the bending radius (r, the radius the VSR coils about during actuation).

Due to the limitation on positioning repeatability of the linear stage, $p_{des}(t)$ is set to a minimum step size of 2.5 mm. The VSR grasps the object placed in the coiling plane as PaCMag applies the magnetic field and the linear stage retracts the nitinol backbone until the set maximum desired tip angle ($\theta_{\text{des}}^{\text{max}} = 220^\circ$) is reached. Beyond this angle as the tip closes the circle, it is not possible to track the tip angle. Hence, the subsequent coiling action is performed by automatically incrementing θ_{des} to complete the grasp. This whole system can also be run in

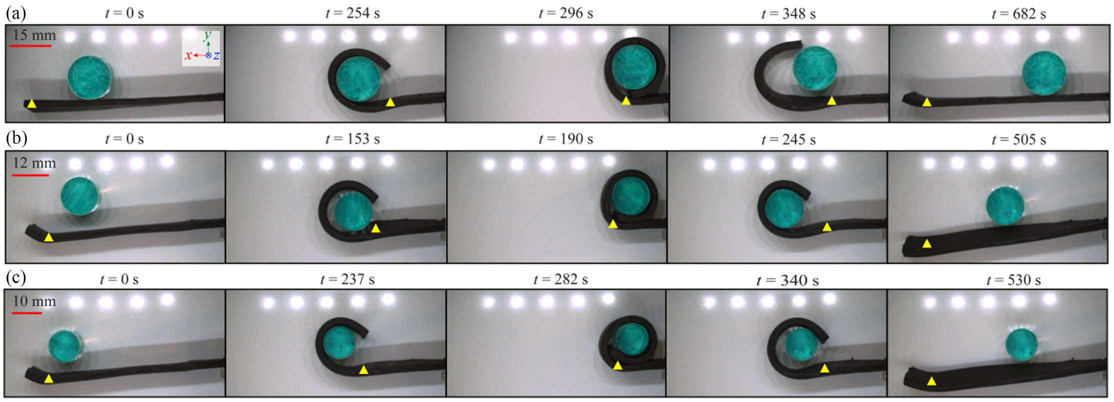

Fig. 8. Closed-loop control demonstration of grasping and releasing objects placed at arbitrary locations and shown at different time instants (t) for three cases: (a) Sample 1 with 15 mm diameter object. (b) Sample 2 with 12 mm object. (c) Sample 2 with 10 mm object. The four stages of the experiment occur between the successive time snippets in the following order: grasping phase; coiling action; uncoiling action; releasing phase. The yellow triangle represents the tip position of the nitinol backbone. Please refer to the supporting video: S3-S5 for the complete demonstration.

reverse to uncoil the VSR and release the entrapped object. Fig. 7 illustrates the complete closed-loop control system.

E. Grasping Force Characterization

A 3-axis force sensor (K3D40, ME-Meßsysteme GmbH, Hennigsdorf, Germany) is used to measure the grasping strength of the VSR. A cylindrical object is attached to the force sensor and the base of the VSR is connected to a linear stage. For different strengths of magnetic fields generated by PaCMag, the VSR is wrapped partially and fully around the object and retracted backwards at small increments using the linear stage. The force sensor records the grasping force on the object along the axial direction of the VSR until the grip fails and the VSR loses contact with the fixed object.

IV. Results

The two VSR samples 1 (7.5 mm bending radius) and 2 (5 mm bending radius) are used to demonstrate the grasping and releasing of printed cylindrical objects in closed-loop as shown in Fig. 8. Three objects of diameters 15, 12 and 10 mm are placed at various locations facing the coiling side of the VSR. The VSR, initially in its straight configuration, wraps around the object to grasp it, coils further to move the object along, then releases the object and uncoils itself to return to its original configuration (Refer to the supporting video: S3-S5 for the complete demonstration). Fig. 9 shows the plots of applied magnetic field ($\mathrm{B}_x, \mathrm{B}_y$), resultant field angle (θ_{act}), position of the nitinol backbone (P), desired tip angle (θ_{des}), and estimated tip angle (θ_{est}). These variables are plotted for sample 1 grasping and releasing the 15 mm object (Fig. 8(a)). The overall control frequency across the three experiments is 1 Hz. The PaCMag coils maintained closed-loop control of the VSR via the visual tip tracking system throughout the "Grasping" and "Releasing" phases of the demonstration (Fig. 9). Visual contact with the tip was lost during the "Coiling" and "Uncoiling" phases as discussed in Section III-C. Here the controller was operating in open-loop. The observed maximum coiling deformation angle owing to the decreasing size of the objects in the three experiments were 360°, 375° and 400°, respectively.

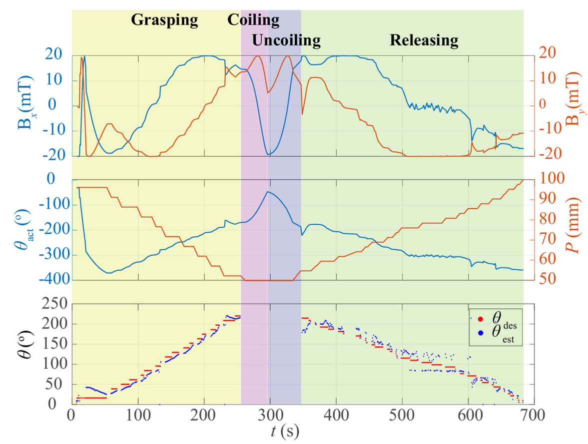

Fig. 9. Results of closed-loop control experiment of Sample 1 grasping and releasing 15 mm object. Plots show the applied magnetic field (B_x, B_y) and its orientation (θ_{act}), position of the nitinol backbone (P), the desired (θ_{des}) and estimated (θ_{est}) tip angles of the VSR during the experiment time (t). The four stages of the experiment occur as follows: grasping phase ($t = 0$–254 s); coiling action ($t = 255$–296 s); uncoiling action ($t = 297$–348 s); releasing phase ($t = 349$–682 s).

The grasping force of VSR sample 2 is characterized at three coiling deformation angles of 360°, 270°, and 180°. The grasping forces at magnetic fields of 30 mT, 20 mT, and 15 mT are measured by the force sensor as the VSR is retracted by the linear stage. Fig. 10 shows the plots of the grasping force along -x-axis (F) as a function of the linear displacement of the VSR (D). It is inferred that the grasping force increases with increasing coiling deformation angle and with increasing magnetic field strength. A maximum grasping force of 1.45 N is obtained for a coiling deformation angle of 360° at a magnetic field of 30 mT.

V. Discussions and Future Work

In this letter, we have demonstrated a proof-of-concept of the grasping and releasing of various diameter cylinders using a variable stiffness magnetically-actuated continuum robot. In doing so we have addressed the non-trivial problem of controlling large

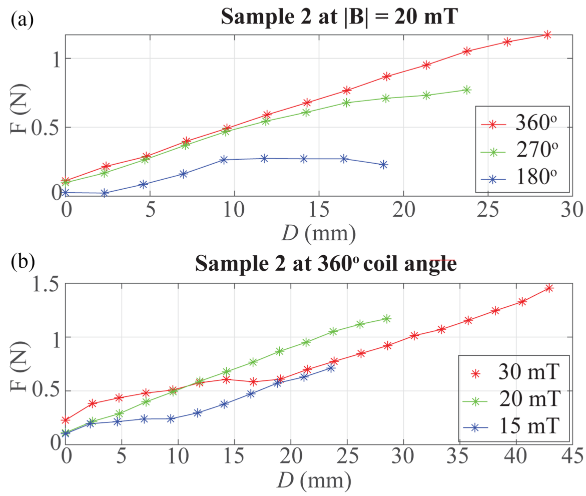

Fig. 10. Results of grasping force characterization of VSR sample 2. Plots show the grasping force along the robot's -x-axis (F) as a function of the linear displacement of the VSR (D) as the coiled robot is stretched along its x-axis for: (a) coil deformation angles of 360°, 270°, and 180° at a magnetic field of 20 mT, (b) coil deformation angle of 360° at magnetic fields of 30 mT, 20 mT, and 15 mT.

(up to $400°$) deformations which, under magnetic actuation, very often display fundamental instabilities. These instabilities are caused by magnetic torque induced by opposite facing magnetic fields which are necessary to drive large elastic deformations as discussed in more detail in [38].

Please see the supporting video: S1 for the demonstration of a failed grasping and releasing experiment of the VSR without the nitinol backbone. We have introduced the concept of a synchronized sliding nitinol backbone with an applied actuating field and proved its feasibility within our VSR to grasp and release various objects. We have also shown that the VSR is able to coil itself into higher energy state equilibrium without relying on anatomical contact forces or interaction with external environment [39]. Supporting video: S2 shows the coiling of the VSR in free space without the influence of any external object.

The results of the grasping force characterization experiments prove that the high coil deformation angles aid in strengthening the VSR. A maximum grasping force of 1.45 N is reported (compared to 0.1 N in [29] and 0.023 N in [30]) and the payload of the VSR is shown to be enhanced by operating at higher magnetic fields.

The maximum grasp strength of a pre-curved (as opposed to magnetically actuated) flexible robot is limited by the elastic properties of the bulk material from which it is fabricated. In the case of a Nitinol tube this elasticity is high (E $\approx$ 50 GPa), but this approach cannot be described as a *soft* robot. In the case of a soft pre-curved robot we will see the grasp strength drop in accordance with the reduction in elastic modulus. The actuating magnetic field allows us to impart a materially useful grasp strength whilst still maintaining a soft elastomeric body.

In order to simplify the demonstration of our feasibility study, we performed our experiments entirely in the horizontal plane (Fig. 8). The VSR is supported in the vertical direction on a smooth acrylic plate thus negating the effects of gravity. Although there are no theoretical issues with the consideration and incorporation of the gravitational force, these simplifications were made on purely practical grounds. Any future study should look to both consider gravity and to control the VSR in unconstrained three dimensional space.

A further simplification worthy of mention pertains to the visual tracking algorithm. Our system locates the tip of the VSR and derives the tip angle to use as a control input. When the VSR wraps into a full circle the tip ceases to be visible, rendering this method of tracking impossible. Any further study should therefore encode a system for tracking the position and size of the circle after a certain deformation angle is achieved. Further ahead, and for a more clinically relevant demonstration, visual tracking is not possible inside the human body so some non-visual sensing method (e.g. medical imaging or strain sensing) should be incorporated.

The bending radius is an interesting parameter worthy of mention here. The radius of the circle around which the robot is magnetized has a profound impact on the achievable radii of the wrapped robot under actuation. If this bending radius is too small the elastic torque will overpower the magnetic torque and the robot will snap open. This can be mitigated to a limited degree with a larger applied field magnitude. Furthermore, if the retraction of the nitinol backbone is not correctly synchronized with the rotation of the applied magnetic field, the actuation descends into the imbalances shown in Fig. 5 and the supporting video. Consequentially, the timing of the retraction of the sliding nitinol backbone is a function of the bending radius (the magnetization) and is enabled by having sufficient magnitude of applied field.

The most obvious limitation of this design is that the backbone is always, when present, straight and the base upon which the VSR is mounted is static. As magnetic actuation is an inherently small scale technology with its most likely applications in minimally invasive surgery (and similar) these constraints limit the current clinical relevance of the design. In order to navigate to any area of interest we should be soft, compliant and mobile. These limitations are by no means definitive however, and the imminent next step is to develop miniaturizable backbones with variably compliant behavior. This would open the door to a truly generalizable grasping VSR. This, however, is non-trivial and one of the significant challenges to the conceptual development of this design. Potential solutions lie in the areas of fluidic actuation [40], phase changing materials [20], electro-statics [41], magneto-rheological fluid [21] and vacuum locking [42] and we intend to explore those options with sufficient potential for miniaturization. Further to this we must also develop a mobile mounting system, such as a manual endoscope, to operate.

We also anticipate developing more reliable and miniaturizable automated fabrication techniques. Although the lower size limit of this design is still an open question, this will allow us to shrink the prototype and potentially incorporate more complex and interesting variable stiffness features.

VI. Conclusion

This letter presents a proof-of-concept of a tongue-like, magnetic variable stiffness coiling robot. This system exploits variable lengthwise mechanical properties to achieve high deformation equilibrium in a way which has not previously been shown. We have demonstrated a closed-loop control strategy to grasp and release objects of varying sizes by synchronizing the sliding nitinol backbone of the robot with the actuating magnetic field. With this contribution we have demonstrated the currently untapped potential of functionalizing variable stiffness magnetically-actuated robots for higher energy state deformations. The variable stiffness grasping robot has potential as a surgical tool for applications in cargo delivery and collection.

Acknowledgment

Any opinions, findings and conclusions, or recommendations expressed in this article are those of the authors and do not necessarily reflect the views of the EPSRC, the ERC or the NWO. For the purpose of open access, the author(s) has applied a Creative Commons Attribution (CC BY) license to any Accepted Manuscript version arising.

References

[1] P. E. Dupont et al., “A decade retrospective of medical robotics research from 2010 to 2020,” *Sci. Robot.*, vol. 6, no. 60, 2021, Art. no. eabi8017.
[2] R. V. Martinez et al., “Robotic tentacles with three–dimensional mobility based on flexible elastomers,” *Adv. Mater.*, vol. 25, no. 2, pp. 205–212, 2013.
[3] J. C. Norton et al., “Intelligent magnetic manipulation for gastrointestinal ultrasound,” *Sci. Robot.*, vol. 4, no. 31, pp. 1–14, 2019.
[4] J. Burgner-Kahrs, D. C. Rucker, and H. Choset, “Continuum robots for medical applications: A survey,” *IEEE Trans. Robot.*, vol. 31, no. 6, pp. 1261–1280, Dec. 2015.
[5] J. Edelmann, A. J. Petruska, and B. J. Nelson, “Magnetic control of continuum devices,” *Int. J. Robot. Res.*, vol. 36, no. 1, pp. 68–85, 2017.
[6] Y. Kim, G. A. Parada, S. Liu, and X. Zhao, “Ferromagnetic soft continuum robots,” *Sci. Robot.*, vol. 4, no. 33, 2019, Art. no. eaax7329.
[7] T. da Veiga et al., “Challenges of continuum robots in clinical context: A review,” *Prog. Biomed. Eng.*, vol. 2, no. 3, Aug. 2020, Art. no. 032003.
[8] R. Zhao, Y. Kim, S. A. Chester, P. Sharma, and X. Zhao, “Mechanics of hard-magnetic soft materials,” *J. Mechanics Phys. Solids*, vol. 124, pp. 244–263, 2019.
[9] Y. Kim and X. Zhao, “Magnetic soft materials and robots,” *Chem. Rev.*, vol. 122, no. 5, pp. 5317–5364, 2022.
[10] E. Diller, J. Zhuang, G. Zhan Lum, M. R. Edwards, and M. Sitti, “Continuously distributed magnetization profile for millimeter-scale elastomeric undulatory swimming,” *Appl. Phys. Lett.*, vol. 104, no. 17, 2014, Art. no. 174101.
[11] G. Z. Lum et al., “Shape-programmable magnetic soft matter,” *Proc. Nat. Acad. Sci.*, vol. 113, no. 41, pp. E6007–E6015, 2016.
[12] G. Pittiglio et al., “Patient-specific magnetic catheters for atraumatic autonomous endoscopy,” *Soft Robot.*, vol. 9, pp. 1120–1133, 2022.
[13] P. Lloyd, O. Onaizah, G. Pittiglio, D. K. Vithanage, J. H. Chandler, and P. Valdastri, “Magnetic soft continuum robots with braided reinforcement,” *IEEE Robot. Automat. Lett.*, vol. 7, no. 4, pp. 9770–9777, Oct. 2022.
[14] J. Zhang, O. Onaizah, K. Middleton, L. You, and E. Diller, “Reliable grasping of three-dimensional untethered mobile magnetic microgripper for autonomous pick-and-place,” *IEEE Robot. Automat. Lett.*, vol. 2, no. 2, pp. 835–840, Apr. 2017.
[15] T. L. Thomas, V. K. Venkiteswaran, G. K. Ananthasuresh, and S. Misra, “Surgical applications of compliant mechanisms: A. review,” *J. Mechanisms Robot.*, vol. 13, no. 2, 2021, Art. no. 020801.
[16] Y. Piskarev et al., “A variable stiffness magnetic catheter made of a conductive phase–change polymer for minimally invasive surgery,” *Adv. Funct. Mater.*, vol. 32, 2022, Art. no. 2107662.
[17] L. Blanc, A. Delchambre, and P. Lambert, “Flexible medical devices: Review of controllable stiffness solutions,” *Actuators*, vol. 6, no. 3, 2017, Art. no. 23.
[18] M. Manti, V. Cacucciolo, and M. Cianchetti, “Stiffening in soft robotics: A review of the state of the art,” *IEEE Robot. Automat. Mag.*, vol. 23, no. 3, pp. 93–106, Sep. 2016.
[19] C. Chautems, A. Tonazzini, D. Floreano, and B. J. Nelson, “A variable stiffness catheter controlled with an external magnetic field,” in *Proc. IEEE/RSJ Int. Conf. Intell. Robots Syst.*, 2017, pp. 181–186.
[20] J. Zhang et al., “Bioinspired continuum robots with programmable stiffness by harnessing phase hange materials,” *Adv. Mater. Technol.*, vol. 8, 2023, Art. no. 2201616.
[21] L. T. Gaeta et al., “Magnetically induced stiffening for soft robotics,” *Soft Matter*, vol. 19, pp. 2623–2636, 2023, doi: 10.1039/D2SM01390H.
[22] Y. Chi, Y. Tang, H. Liu, and J. Yin, “Leveraging monostable and bistable pre-curved bilayer actuators for high-performance multitask soft robots,” *Adv. Mater. Technol.*, vol. 5, no. 9, 2020, Art. no. 2000370.
[23] Y. Dong et al., “Untethered small-scale magnetic soft robot with programmable magnetization and integrated multifunctional modules,” *Sci. Adv.*, vol. 8, no. 25, 2022, Art. no. eabn8932.
[24] S. Miyashita, S. Guitron, K. Yoshida, S. Li, D. D. Damian, and D. Rus, “Ingestible, controllable, and degradable origami robot for patching stomach wounds,” in *Proc. IEEE Int. Conf. Robot. Automat.*, 2016, pp. 909–916.
[25] R. Manickam, S. Nachimuthu, S. Kallappan, and M. Pai, “Laparoscopic adenomectomy in BPH - does it have a role today?,” *Asian J. Urol.*, vol. 5, pp. 37–41, 2018.
[26] T. Xu, J. Zhang, M. Salehizadeh, O. Onaizah, and E. Diller, “Millimeter-scale flexible robots with programmable three-dimensional magnetization and motions,” *Sci. Robot.*, vol. 4, no. 29, 2019, Art. no. eaav4494.
[27] A. Mehrkish and F. Janabi-Sharifi, “A comprehensive grasp taxonomy of continuum robots,” *Robot. Auton. Syst.*, vol. 145, 2021, Art. no. 103860.
[28] N. Giri and I. Walker, “Continuum robots and underactuated grasping,” *Mech. Sci.*, vol. 2, pp. 51–58, 2011.
[29] J. Sikorski, E. S. Rutting, and S. Misra, “Grasping using magnetically-actuated tentacle catheter: A proof-of-concept study,” in *Proc. IEEE 7th Int. Conf. Biomed. Robot. Biomechatron.*, 2018, pp. 609–614.
[30] V. K. Venkiteswaran, D. K. Tan, and S. Misra, “Tandem actuation of legged locomotion and grasping manipulation in soft robots using magnetic fields,” *Extreme Mechanics Lett.*, vol. 41, 2020, Art. no. 101023.
[31] A. Moss and K. Nalankilli, “Standardisation of polypectomy technique,” *Best Pract. Res. Clin. Gastroenterol.*, vol. 31, no. 4, pp. 447–453, 2017.
[32] V. K. Venkiteswaran, J. Sikorski, and S. Misra, “Shape and contact force estimation of continuum manipulators using pseudo rigid body models,” *Mechanism Mach. Theory*, vol. 139, pp. 34–45, 2019.
[33] P. Lloyd, G. Pittiglio, J. H. Chandler, and P. Valdastri, “Optimal design of soft continuum magnetic robots under follow-the-leader shape forming actuation,” in *Proc. IEEE Int. Symp. Med. Robot.*, 2020, pp. 111–117.
[34] T. Da Veiga et al., “Material characterization for magnetic soft robots,” in *Proc. IEEE 4th Int. Conf. Soft Robot.*, 2021, pp. 335–342.
[35] P. Lee, Y. Chen, J. Hu, and C. Chang, “Comparison of mechanical stability of elastic titanium, nickel-titanium, and stainless steel nails used in the fixation of diaphyseal long bone fractures,” *Materials*, vol. 11, pp. 1–11, 2018.
[36] T. L. Thomas, J. Sikorski, G. Ananthasuresh, V. K. Venkiteswaran, and S. Misra, “Design, sensing, and control of a magnetic compliant continuum manipulator,” *IEEE Trans. Med. Robot. Bionics*, vol. 4, no. 4, pp. 910–921, Nov. 2022.
[37] M. Cheriet, N. Kharma, C. Suen, and C.-L. Liu, *Character Recognition Systems: A. Guide for Students and Practitioners*. Hoboken, NJ, USA: Wiley, 2007.
[38] P. Lloyd, Z. Koszowska, M. Di Lecce, O. Onaizah, J. H. Chandler, and P. Valdastri, “Feasibility of fiber reinforcement within magnetically actuated soft continuum robots,” *Front. Robot. AI*, vol. 8, 2021, Art. no. 715662.
[39] T. L. Bruns et al., “Magnetically steered robotic insertion of cochlear-implant electrode arrays: System integration and first-in-cadaver results,” *IEEE Robot. Automat. Lett.*, vol. 5, no. 2, pp. 2240–2247, Apr. 2020.
[40] T. Liu, H. Xia, D.-Y. Lee, A. Firouzeh, Y.-L. Park, and K.-J. Cho, “A positive pressure jamming based variable stiffness structure and its application on wearable robots,” *IEEE Robot. Automat. Lett.*, vol. 6, no. 4, pp. 8078–8085, Oct. 2021.
[41] S. Hoh, T. Helps, R. S. Diteesawat, M. Taghavi, and J. Rossiter, “Electro-lattice actuator: A compliant high-contractile active lattice structure,” *Smart Mater. Struct.*, vol. 30, no. 12, Nov. 2021, Art. no. 125034.
[42] Y.-J. Kim, S. Cheng, S. Kim, and K. Iagnemma, “A novel layer jamming mechanism with tunable stiffness capability for minimally invasive surgery,” *IEEE Trans. Robot.*, vol. 29, no. 4, pp. 1031–1042, Aug. 2013.